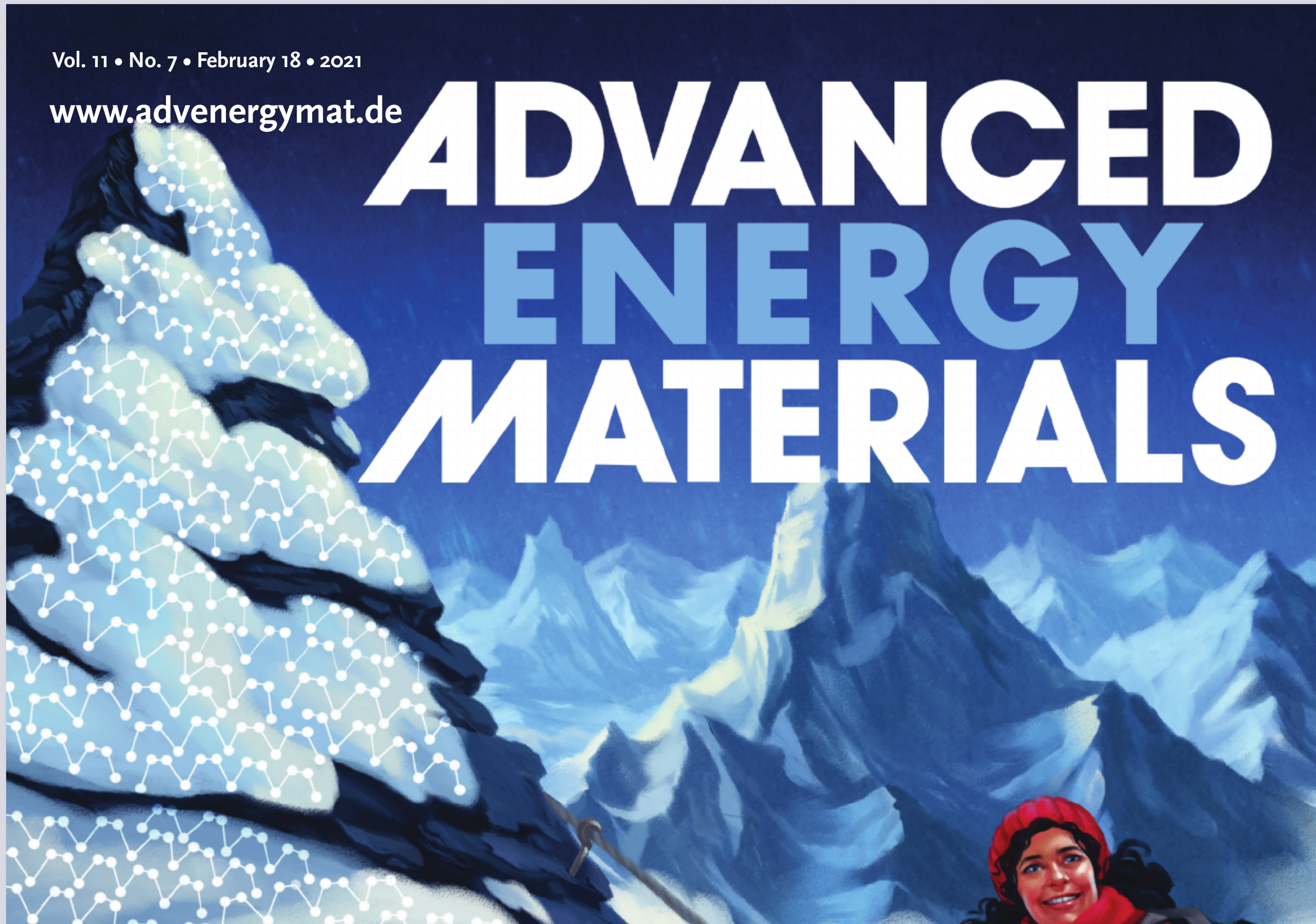




Vol. 11 • No. 7 • February 18 • 2021

www.advenergymat.de

ADVANCED ENERGY MATERIALS



Alloying of Alkali Metals with Tellurene

Rishabh Jain, Yifei Yuan, Yashpal Singh, Swastik Basu, Dawei Wang, Aijun Yang, Xiaohua Wang, Mingzhe Rong, Ho Jin Lee, David Frey, Rajan Khadka, Prateek Hundekar, Sang Ouk Kim, Fudong Han, Lin-Wang Wang, David Mitlin, Reza Shahbazian-Yassar, and Nikhil Koratkar*

Graphite anodes offer low volumetric capacity in lithium-ion batteries. By contrast, tellurene is expected to alloy with alkali metals with high volumetric capacity ($\approx 2620 \text{ mAh cm}^{-3}$), but to date there is no detailed study on its alloying behavior. In this work, the alloying response of a range of alkali metals ($A = \text{Li, Na, or K}$) with few-layer Te is investigated. In situ transmission electron microscopy and density functional theory both indicate that Te alloys with alkali metals forming $A_2\text{Te}$. However, the crystalline order of alloyed products varies significantly from single-crystal (for Li_2Te) to polycrystalline (for Na_2Te and K_2Te). Typical alloying materials lose their crystallinity when reacted with Li—the ability of Te to retain its crystallinity is therefore surprising. Simulations reveal that compared to Na or K, the migration of Li is highly “isotropic” in Te, enabling its crystallinity to be preserved. Such isotropic Li transport is made possible by Te’s peculiar structure comprising chiral-chains bound by van der Waals forces. While alloying with Na and K show poor performance, with Li, Te exhibits a stable volumetric capacity of $\approx 700 \text{ mAh cm}^{-3}$, which is about twice the practical capacity of commercial graphite.

capacity of $\approx 2620 \text{ mAh cm}^{-3}$ when alloyed with Lithium (Li). However, bulk tellurium has low ionic and electrical conductivity^[2] and is not well suited for Li-ion batteries (LIBs). By contrast, Li ion diffusion and charge transport limitations could be mitigated in few-layer Te flakes due to their reduced thickness. In fact, Te has many attractive features when compared to other materials in the 2D family.^[5] For example, unlike 2D transition metal dichalcogenides and hexagonal boron nitride, Te displays fast charge carrier mobility ($\approx 10^3 \text{ cm}^2 \text{ V}^{-1} \text{ s}^{-1}$).^[6,7] Further, unlike phosphorene and silicene which are easily oxidized, Te is stable under ambient conditions.^[8–11] Importantly, few-layered Te flakes can be manufactured using the hydrothermal method with controllable thickness and with a high yield of $\approx 98\%$.^[5] All of these attributes render Te a promising anode material for LIB applications.

Despite this, there is no study reported to

date on the alloying behavior of 2D sheets of Te with Li.

In this work, we have investigated how few-layer Te reacts with a range of alkali metals including Li, sodium (Na), and potassium (K). In situ transmission electron microscopy (TEM)

1. Introduction

Tellurene (Te) is the 2D allotrope of bulk tellurium.^[1,2] Bulk tellurium is predicted^[3,4] to deliver a high volumetric specific

R. Jain, P. Hundekar, Prof. F. Han, Prof. N. Koratkar
Department of Mechanical
Aerospace and Nuclear Engineering
Rensselaer Polytechnic Institute
110 8th Street, Troy, NY 12180, USA
E-mail: koratn@rpi.edu

Dr. Y. Yuan, Prof. R. Shahbazian-Yassar
Department of Mechanical and Industrial Engineering
the University of Illinois at Chicago
Chicago, IL 60607, USA

Dr. Y. Singh, Dr. L.-W. Wang
Material Science Division
Lawrence Berkeley National Laboratory
Berkeley, CA 94720, USA


Dr. S. Basu, Prof. D. Mitlin
Mechanical Engineering Department
University of Texas
Austin, TX 78712, USA

D. Wang, Dr. A. Yang, Prof. X. Wang, Prof. M. Rong
State Key Laboratory of Electrical Insulation and Power Equipment
Xi'an Jiaotong University
No 28 Xianning West Road, Xi'an 710049, China

H. J. Lee, Prof. S. O. Kim
National Creative Research Initiative (CRI) Center for
Multi-dimensional Directed Nanoscale Assembly
Department of Materials Science and Engineering
KAIST
Daejeon 34141, Republic of Korea

D. Frey
Center for Materials
Devices, and Integrated Systems
Rensselaer Polytechnic Institute
110 8th Street, Troy, NY 12180, USA

R. Khadka, Prof. N. Koratkar
Department of Materials Science and Engineering
Rensselaer Polytechnic Institute
110 8th Street, Troy, NY 12180, USA

 The ORCID identification number(s) for the author(s) of this article can be found under <https://doi.org/10.1002/aenm.202003248>.

DOI: 10.1002/aenm.202003248

and density functional theory (DFT) calculations indicate that few-layer Te reacts with alkali atoms ($A = \text{Li, Na, and K}$) to form the alloy phase (Li_2Te , Na_2Te , and K_2Te). Surprisingly, a “single-crystal” Li_2Te alloying product was obtained, which is very rare during alloy formation, in comparison with polycrystalline Na_2Te and K_2Te . In fact, all common nanomaterials used in LIBs such as nano-silicon,^[12] nano-tin,^[13] and phosphorene^[14] as well as their bulk counterparts^[14,15] undergo a crystalline to polycrystalline or amorphous transition on lithiation. Our calculations using the nudged elastic band (NEB) method reveal significantly lower energy barrier for Li migration in Te (≈ 0.13 eV) when compared with Na migration (≈ 0.32 eV) and K migration (≈ 0.62 eV). NEB further reveals nearly equal energy barrier for Li migration in both “across-belt” and “along-belt” directions in the Te lattice, which is not the case for Na or K migration. Further, ab-initio molecular dynamics (AI-MD) indicates nearly equal mean square displacement (MSD) of Li along the across- and along-belt directions, confirming “isotropic” movement of Li atom in the interior of the few-layer Te. Such isotropic transport was not observed for either Na or K atoms. We present a hypothesis to explain why the isotropic transport of Li within Te enables retention of its single-crystalline nature. Such preservation of single-crystal structure could have important practical implications, since it mitigates cell degradation related to secondary grains or particles such as microcracks, as has been well documented for single-crystal layered transition metal oxide cathodes.^[16]

To examine the performance of the Te electrode, we assembled and tested half cells of Te versus Li/Na/K metal. Due to high volume expansion during alloy formation with Li ($\approx 170\%$), Na ($\approx 280\%$), and K ($\approx 420\%$), significant capacity fade was observed, especially for Na and K. In the case of Li, the capacity also reduces but stabilizes at ≈ 700 mAh cm^{-3} , which is about twice the practical volumetric capacity ($330\text{--}430$ mAh cm^{-3}) of commercial (battery-grade) graphite.^[17] We further demonstrate that the capacity fade can be mitigated in a Te/graphene composite electrode by using graphene as a buffer material to suppress the pulverization of Te. These results demonstrate that Te can be a promising anode material for LIB applications, especially in situations where high volumetric performance is desired such as for electricity (grid) storage. Our study also provides new fundamental insight as to why certain alloying materials are able to preserve their crystallinity when deployed in batteries.

2. Results

2.1. Synthesis of Tellurene

Experimental methods for the synthesis of 1D tellurium have been well researched and are categorized into either vapor phase or solution phase processes.^[18,19] Conversely, the synthesis of 2D Te is not well established. Prior works showed growth of Te on various substrates such as mica,^[20] highly orientated graphite,^[21] and graphene/SiC substrates^[22] using van der Waals (vdW) epitaxy method. The conventional liquid phase exfoliation method has also been employed for the synthesis of Te.^[23] However, such methods face critical challenges in terms

of scalability, control over thickness, substrate-free growth, and sensitivity to growth conditions, which inhibits its application, especially for energy storage where scalable manufacturing is essential.^[5] However, recently developed hydrothermal methods^[1,2] show promise to overcome these limitations, and were used in this study for synthesis of Te (grey colored powder, inset of Figure 1a) (details regarding the growth mechanism and procedures are provided in the Experimental Section).

Scanning electron microscopy (SEM) and TEM confirmed the presence of a sheet-like structure with lateral dimensions ranging from $10\text{--}30$ μm (Figure 1a,c). Selected area diffraction pattern (SAED) confirmed the high crystallinity of as-synthesized Te (Figure 1d). The typical thickness of a Te flake was ≈ 20 nm, obtained using atomic force microscopy (AFM) (Figure 1b). This corresponds to ≈ 45 layers (considering inter-layer spacing of 0.445 nm for Te). Raman spectroscopy of as-synthesized Te shows three active modes: E_1 mode (≈ 90.8 cm^{-1}), A_1 mode (≈ 120.3 cm^{-1}), and E_2 mode (≈ 140.7 cm^{-1}) (Figure 1e) which is consistent with literature.^[1] Chemical composition analysis of as-synthesized Te was obtained using X-ray photoelectron spectroscopy (XPS). De-convoluted XPS analysis of Te 3d showed the presence of two major peaks at ≈ 571.39 eV and ≈ 581.86 eV, which are attributed to the $3d_{5/2}$ and $3d_{3/2}$ spin-orbital doublets of Te–Te bond, respectively (Figure 1f). Two small peaks appearing at ≈ 574.73 eV and ≈ 585 eV are attributed to the Te–O bond (slight oxidation of Te is inevitable during the hydrothermal process). X-ray diffraction (XRD) further confirmed the presence of highly crystalline Te (Figure 1g), which is consistent with previous studies.^[2] It should be noted that three possible phases of Te have been predicted theoretically; α -Te, β -Te, and γ -Te, among which α -Te and β -Te are the most stable phases.^[24] These theoretical reports also indicate that few-layer Te acquires the α phase, while monolayer Te exhibits the β phase. In our work, morphological analysis, Raman spectra, and AFM all reveal the presence of few-layered Te, which indicates that the as-synthesized Te is in the α phase (simulated structure is shown in Figure 1h).

2.2. Understanding Alkalization of Te Using In Situ Transmission Electron Microscopy Supported by Density Functional Theory

In situ TEM has proved to be successful in understanding the major electrochemical mechanisms^[25,26] (i.e., intercalation, alloying, and conversion) that an anode material could undergo during ion insertion/extraction. Especially for alloying/de-alloying reactions, in situ TEM provides useful information related to volume expansion, change in morphology, and change in crystallinity that the alloying material undergoes.^[26] In this work, we used in situ TEM to study the alloying of Te with Li, Na as well as K. Figure S1, Supporting Information, shows a schematic of the in situ TEM setup used to study the alkalization (lithiation/sodiation/potassiation) of few-layer Te, wherein the corresponding alkali metal (Li/Na/K) was used as the counter electrode, naturally grown metal oxide layer (i.e., lithium oxide, sodium oxide, or potassium oxide) as a solid-state electrolyte, and Te as the working electrode with gold (Au) or tungsten (W) as the current collectors. A constant bias

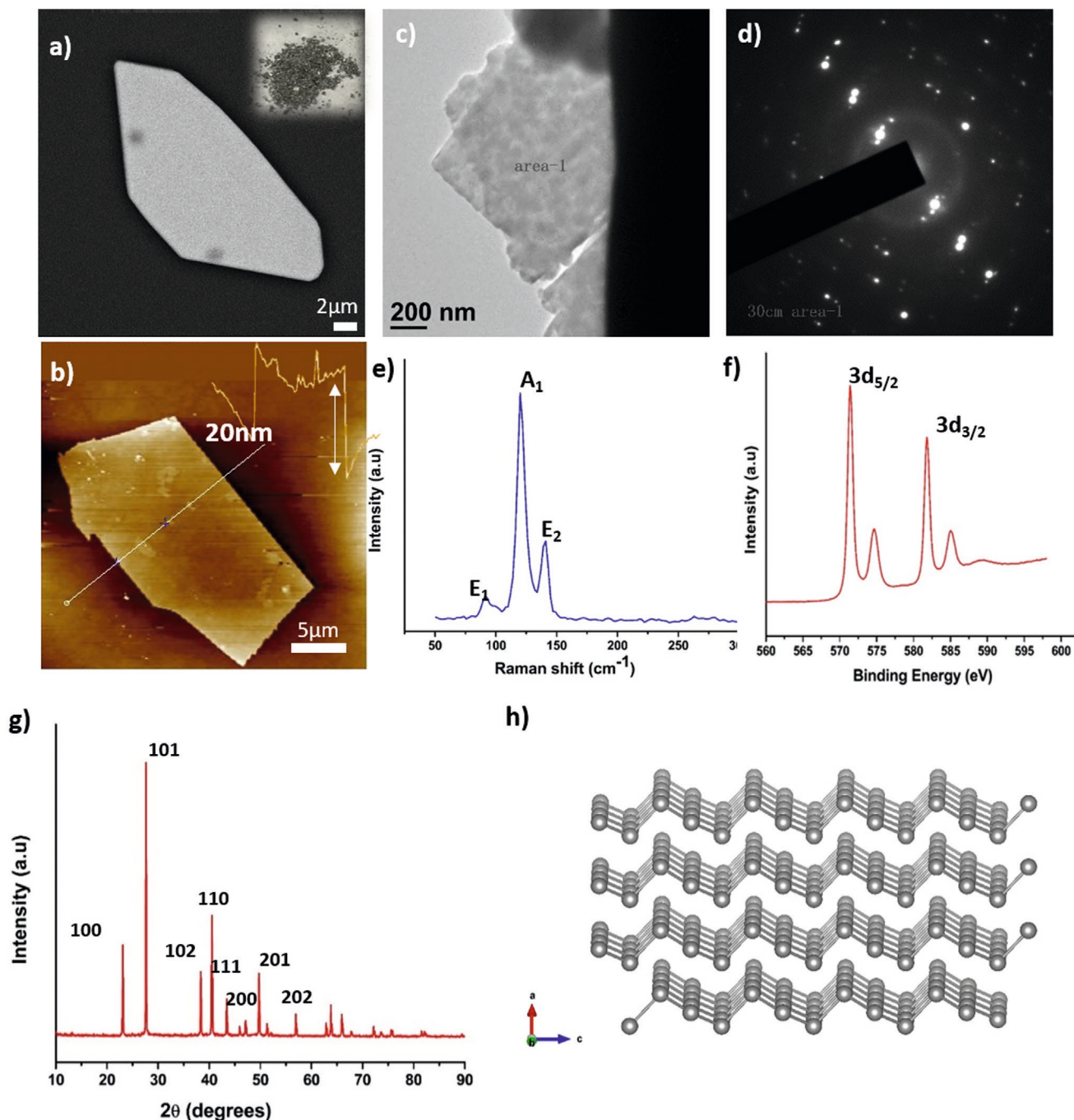


Figure 1. Characterization of Te produced by hydrothermal synthesis. a) SEM imaging, b) AFM imaging, c) TEM, d) SAED pattern, e) Raman spectra, f) High-resolution Te 3d XPS spectra, g) XRD spectra, and h) 3D illustration of the few-layer Te structure.

voltage (≈ 3 V) is applied to initiate insertion of metal ions into Te. To understand the alloying mechanism, TEM images were taken during the alkalization of Te at different time intervals. The real-time TEM imaging indicates that the few-layer Te flake gradually slides and expands during Li insertion (Figure 2a–d and Movie S1, Supporting Information). No significant delamination of Te from the W current collector was observed. Surprisingly, unlike other alloy-based materials, Te expands almost “isotropically” in both x - ($\approx 11\%$) and y -directions ($\approx 10\%$) till

full lithiation.^[25,27–29] SAED and theoretical calculations were employed to understand the phase information of the alloyed product (i.e., Li_xTe). Te can form three different alloy compositions with Li (LiTe_3 , Li_2Te , and Li_3Te). SAED pattern of pure Te and Li_xTe is shown in Figure 2e,f, wherein pure Te shows a bright spot related to (100) plane with d spacing of ≈ 3.9 Å. In addition, a diffused halo is discernible in the background, which is attributed to oxidation (Figure 1f) of Te, which is unavoidable in hydrothermal synthesis (as discussed in previous

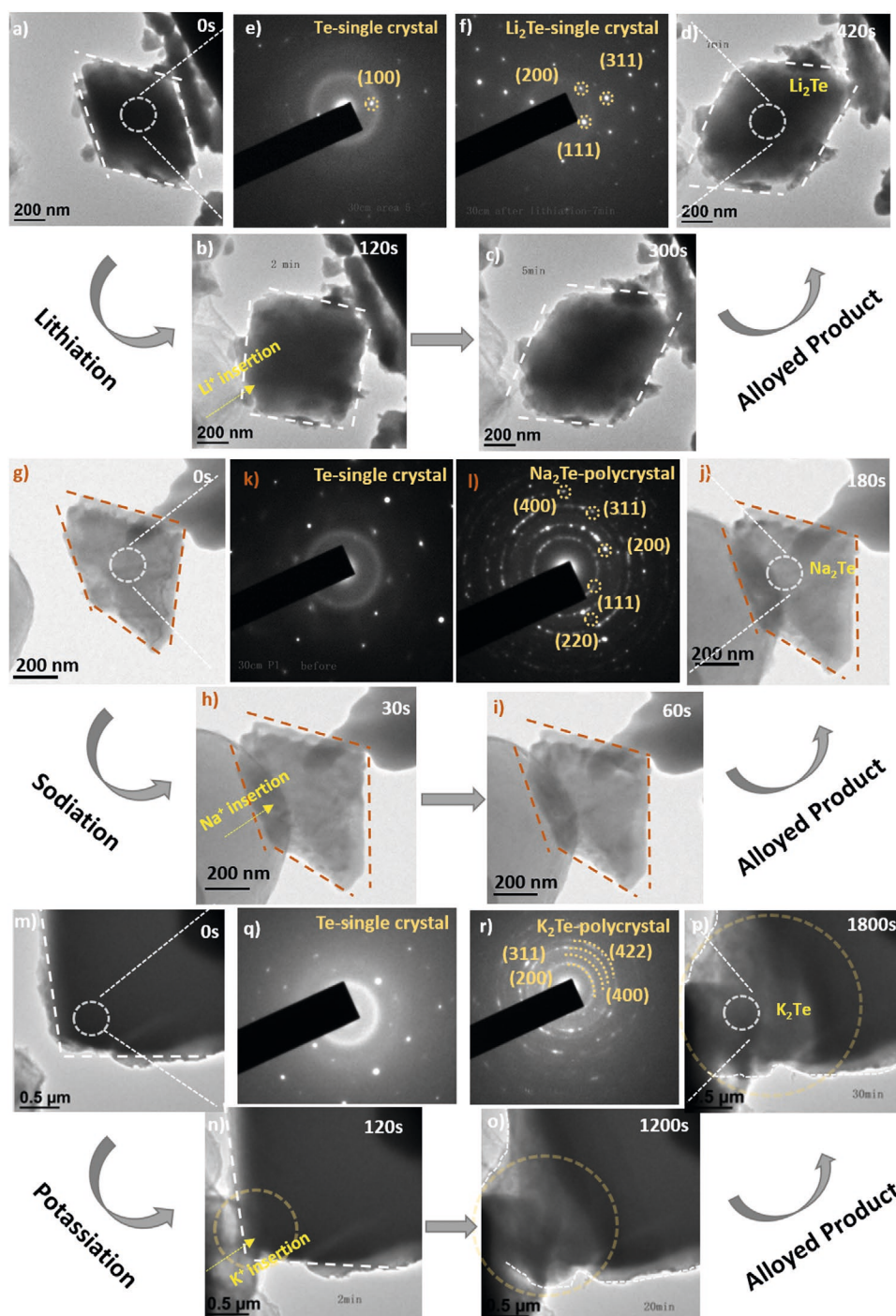


Figure 2. In situ TEM study of alkali ion insertion in Te. TEM images of Te a) before (0 s) and after b) 120 s, c) 300 s, and d) complete (420 s) lithium ion insertion. Corresponding SAED patterns of e) pristine Te and f) lithiated Te. TEM images of Te g) before (0 s) and after h) 30 s, i) 60 s, and j) complete (180 s) sodium ion insertion. Corresponding SAED patterns of k) pristine Te and l) sodiated Te. TEM images of Te m) before (0 s) and after n) 120 s, o) 1200 s, and p) complete (1800 s) potassium ion insertion. Corresponding SAED patterns of q) pristine Te and r) potassiated Te.

section). The SAED pattern of Li_xTe shows three different bright spots at d spacing of ≈ 3.8 , 3.27 , and 2.09 Å which matches well with the diffraction plane (111), (200), and (311) of Li_2Te , respectively. Interestingly, the diffraction pattern of Li_2Te did not exhibit rings, confirming that the lithiation of Te leads to the formation of a “crystalline” Li_2Te alloy. This is a striking

result since almost all of the known alloy-based anode materials, such as Si, Al, Sn, and P, form either polycrystalline or amorphous materials on lithiation.^[12–14] To check for reproducibility, the SAED analysis was repeated at several locations on the alloyed sample, which confirmed the single-crystalline property of Li_2Te (Figure S2, Supporting Information). Since

Te remains single-crystal both before and after the lithiation step, we expect that the Te flakes also remain single-crystalline during the lithiation process.

We used DFT calculations to calculate the formation energy per Te atom of all the possible alloys, among which Li_2Te showed a lower formation energy (-3.19 eV) as compared to LiTe_3 (-0.38 eV) and Li_3Te (-3 eV) (Figure S3, Supporting Information). This indicates that Li_2Te is the expected alloy, which is consistent with our SAED results. Volume expansion due to alloy formation was theoretically calculated ($\approx 175.80\%$), which indicated that 2D Te expands primarily in the z -direction ($\approx 119\%$) (Figure S6, Supporting Information). A similar set of studies were employed to study sodiation of Te. Figure 2g shows pure Te before Na insertion and Figure 2j shows fully sodiated tellurene (Na_xTe). The different time scale in Na insertion in comparison to Li may be due to variation in size or thickness of the Te flake that was used or differences in the diffusion rate of ions. Unlike Li insertion, Te expands “anisotropically” in the x - ($\approx 20\%$) and y - ($\approx 8\%$) directions until full sodiation (Figure 2g–j and Movie S2, Supporting Information). SAED pattern of pure Te confirms its single-crystal property before insertion of Na, whereas SAED pattern of Na_xTe shows diffused rings with bright spots at d spacing of ≈ 4.5 , 3.35 , 2.59 , and 2.22 Å which matches with the diffraction plane (111), (200), (220), and (311) of Na_2Te , respectively (Figure 2k,l). The appearance of diffused rings indicates that the alloying of Te with Na leads to the formation of polycrystalline Na_2Te . Formation energy per Te atom was calculated (Figure S4, Supporting Information) for all possible stable alloys of Te with Na (NaTe_3 , NaTe , and Na_2Te) among which Na_2Te showed lower formation energy (-2.83 eV) than NaTe_3 (-0.55 eV) and NaTe (-1.48 eV), which is consistent with the SAED characterization. Volume expansion of Te during sodiation (Figure S6, Supporting Information) was $\approx 286.5\%$, with the primary expansion occurring in the z -direction ($\approx 190\%$).

In the case of potassiation, Te expands even more anisotropically, in the x -direction ($\approx 40\%$) and y -direction ($\approx 15\%$), when compared to sodiation (Figure 2m–p and Movie S3, Supporting Information). SAED pattern of potassiated Te (K_xTe) shows various diffused rings with few bright spots at d spacing of ≈ 4.14 , ≈ 2.45 , ≈ 2.08 , and ≈ 1.62 Å which matches with the diffraction plane (200), (311), (400), and (422) of K_2Te , respectively (Figure 2q,r). The presence of diffused rings indicates that the K_2Te product is polycrystalline. K_2Te showed lower formation energy per Te atom (-3.09 eV) than other stable alloys such as KTe (-1.71 eV), KTe_3 (-0.19 eV), K_2Te_3 (-1.24 eV), and K_5Te_3 (-2.69 eV) (Figure S5, Supporting Information) which confirms that the potassiation of Te leads to the formation of K_2Te . Volume expansion during alloy formation from Te to K_2Te was $\approx 474.74\%$ (Figure S6, Supporting Information), with a massive volume expansion in the z -direction ($\approx 280\%$). From the above results, it is evident that alkali (A) ion (Li/Na/K) insertion into few-layer Te led to the formation of an A_2Te (Li_2Te , Na_2Te , and K_2Te) alloy wherein the alloyed material crystallinity changed from single-crystal (for Li_2Te) to poly-crystal (for Na_2Te and K_2Te). The volume expansion in the material followed an increasing trend with increase in size of A from $\approx 175\%$ for Li to $\approx 474\%$ for K.

3. Discussion

3.1. Adsorption and Charge Transfer Analysis

DFT calculations were used to study the adsorption, charge transfer, and diffusion of alkali ions in few-layer Te. First, we studied the surface loading of Li/Na/K on 2D Te sheets. In the second step, we investigated the diffusion of these ions “across” and “along” the belts of Te sheets (Figure 3a). Optimized few-layer (four layers) of Te (Figure S7a–c, Supporting Information) acquires the α phase, consistent with previous studies.^[24] Unlike other 2D materials (e.g., graphene, MoS_2 , or WS_2), the Te structure is highly anisotropic such that a Te atom is bonded to another Te atom only in one direction (along-belt direction). Multilayer Te has an ABAB stacking with an interlayer distance of ≈ 4.44 Å. Within a layer, Te atoms make two bonds with other Te atoms with bond length ranging from 2.83 Å ($\text{Te1}-\text{Te2}$) to ≈ 2.9 Å ($\text{Te1}-\text{Te3}$) and width of the belt is ≈ 4.43 Å (distance between $\text{Te1}-\text{Te4}$) (Figure S7d, Supporting Information). The corresponding bond angle ranges from $\approx 101.3^\circ$ to 101.8° . After the structural optimization of Te, Li/Na/K ions were sampled at different sites on the top surface of Te and allowed to relax. Our calculations indicate that the space between two belts provides stronger binding site for ions (Figure S8, Supporting Information). Distances between Li and the closest Te atoms are ≈ 2.72 Å ($\text{Li}-\text{Te1}$), ≈ 2.75 Å ($\text{Li}-\text{Te2}$), and ≈ 2.82 Å ($\text{Li}-\text{Te3}$) (Figure S8a–c and Table S1, Supporting Information).

In case of Na, distances are ≈ 3.05 Å ($\text{Na}-\text{Te1}$), ≈ 3.12 Å ($\text{Na}-\text{Te2}$), and ≈ 3.09 Å ($\text{Na}-\text{Te3}$) (Figure S8d–f and Table S1, Supporting Information). For K, distances increase further and are ≈ 3.41 Å ($\text{K}-\text{Te1}$), ≈ 3.61 Å ($\text{K}-\text{Te2}$), and ≈ 3.4 Å ($\text{K}-\text{Te3}$) (Figure S8g–i and Table S1, Supporting Information). It is to be noted that no significant disruptions were observed due to ion adsorption on the surface of Te. Energy shift of alkali ion/Te complex with vertical distance of the alkali ion to the Te surface was also calculated (Figure S9, Supporting Information). The energy of the system remained constant beyond 7 Å but showed a rapid decline below 6 Å, which indicates a strong interaction between alkali atoms and Te and confirms the absence of any energy barrier for the loading process. The adsorption energy of Li/Na/K (E_{ab}) on the surface of the 2D Te sheet was calculated using the following equation:

$$E_{\text{ab}} = E_{\text{Te-Li/Na/K}} - E_{\text{Te}} - \mu_{\text{Li/Na/K}} \quad (1)$$

where $E_{\text{Te-Li/Na/K}}$, E_{Te} , and $\mu_{\text{Li/Na/K}}$ refer to total energies of Li/Na/K adsorbed on Te, Te, and the chemical potential of Li/Na/K atom, respectively. The chemical potential of alkali atoms was calculated in two ways: 1) considering a single isolated atom in a cell (μ_{atom}), and 2) considering the bulk phase of alkali metal (μ_{bulk}). The conventional view is to calculate E_{ab} by considering a single isolated alkali atom. However, recent reports suggest that considering a bulk phase of alkali atom is more appropriate (especially in the battery field).^[30,31] Herein, we have considered both the methods and observed that the binding energies of Li/Na/K with the surface of Te are all negative (Figure 3b and Table S1, Supporting Information) which indicates a favorable interaction. However, we do observe a difference in the binding energy trend wherein Li adsorbed more strongly (-2.56 eV)

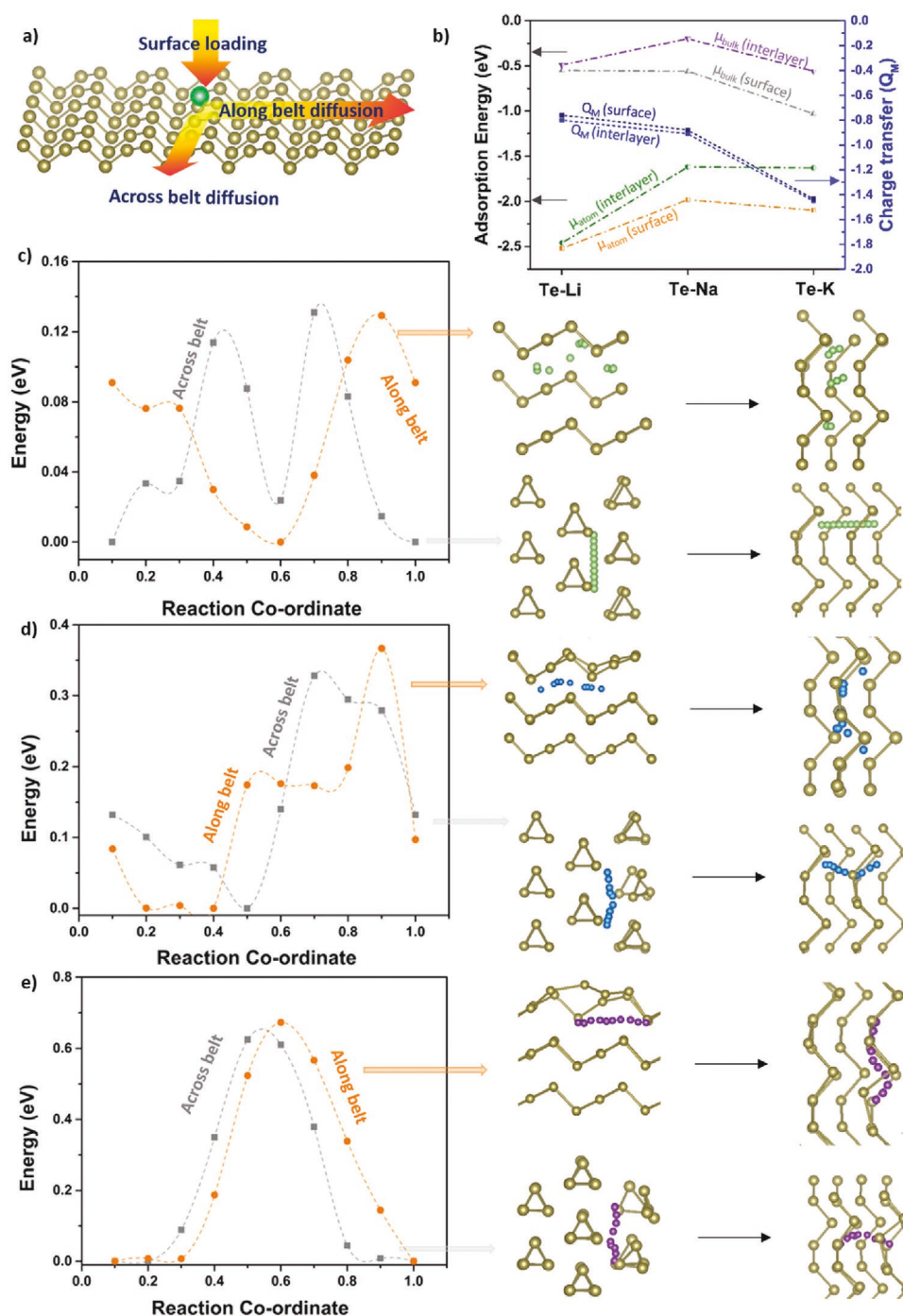


Figure 3. DFT study of interaction between Te and alkali ions. a) Schematic illustration of alkali atom adsorption and diffusion through the "along-belt" and "across-belt" directions. b) Adsorption energy of different alkali atoms on the surface and in the interior of Te, calculated using μ_{atom} and μ_{bulk} method and charge transfer between alkali ions and Te sheets. c–e) Diffusion energy barrier "along-belt" and "across-belt" for c) Li, d) Na, and e) K migration in interior of few-layered Te. Corresponding simulated structures are also shown.

than other alkali atoms (−1.98 eV for Na and −2.1 eV for K) based on μ_{atom} method, but with the μ_{bulk} method, K adsorbed more strongly (−1.028 eV) than Li (−0.55 eV) and Na (−0.56 eV) (Table S1, Supporting Information).

Similar calculations were repeated with alkali atoms (Li/Na/K) in between two layers (Figure S10 and Table S1,

Supporting Information). No significant disruption was observed in the case of Li inside two layers (Figure S10a–c, Supporting Information). However, significant damage and complete disruption of the upper layer was observed in the case of Na/K due to their larger size when compared to the Li atom (Figure S10d–i, Supporting Information). This indicates that

delamination of the electrode is less severe for a Te anode with Li insertion as opposed to Na or K. Similarly, the magnitude of the binding energy of Li when placed between two layers did not decrease significantly (≈ 0.05 eV) in comparison with Na (≈ 0.36 eV) and K (≈ 0.5 eV), which suggests that the thermodynamic barrier for the transport of Li through Te layers is much lower than for Na and K. Hirschfeld I-charge analysis was further employed to illustrate the spatial charge distribution between alkali atoms and Te. Charge deficiency on alkali atoms and excess charge on Te indicates charge transfer from alkali atoms to the surface of Te. Hirschfeld I-charge analysis indicates that Li transfers $0.8 e^-$ to Te, which is lower than Na ($0.911 e^-$) and K ($1.45 e^-$) (Figure 3b). This is due to the low ionization energy of K in comparison with Na and Li. A similar trend in charge transfer was also observed for alkali atom adsorption in between Te sheets. The effect of alkali ion absorption on Te was further analyzed by calculating the total density of states (TDOS). The TDOS of pristine Te shows a bandgap of ≈ 0.3 eV with Fermi level close to the valence band indicating p-type semiconducting behavior of Te, which is in agreement with previous reports^[2] (Figure S11a, Supporting Information). On alkali ion adsorption over Te, the Fermi level shifts inside the conduction band, thus showing metallic behavior due to n-type doping induced by the alkali atom (Figure S11b–d, Supporting Information). Our DFT calculations therefore indicate effective absorption of alkali ions on Te, with significant charge transfer and semiconductor to metallic transition, all favorable characteristics for a battery electrode material.

3.2. Diffusion of Alkali Atoms on Monolayer Tellurene

The mobility of alkali ions inside the electrode material not only governs the rate performance of the battery but also helps us in understanding the evolution of electrode structure during the alloying reaction. NEB calculations were employed to evaluate energy barrier for the diffusion of all three alkali ions in the “along-belt” and “across-belt” directions of single-layer Te and in the interior of few-layered Te (Experimental Section). After establishing the most stable site for alkali ion adsorption on single-layer Te, we studied migration of the alkali ion from one stable site to the next for three possible pathways: 1) across-belt, 2) along-belt, and 3) through the single-layer Te sheet (Figure S12, Supporting Information). While studying migration across-belt, we observed that all three alkali atoms showed one major peak at the same reaction co-ordinate with energy barrier for Li (0.19 eV, Figure S12a, Supporting Information), Na (0.19 eV, Figure S12b, Supporting Information), and K (0.13 eV, Figure S12c, Supporting Information). Such difference can possibly arise due to the larger distance of K atom from Te surface (4.07 Å) in comparison with Li (2.92 Å) and Na atom (3.47 Å), which can lead to less hindrance for Te atoms during K migration. However, in case of “along-belt” diffusion, energy barrier for Li migration (≈ 0.2 eV, Figure S12a, Supporting Information) is less than Na (≈ 0.32 eV, Figure S12b, Supporting Information) and K (≈ 0.33 eV, Figure S12c, Supporting Information) and exhibits a peak at a different reaction co-ordinate in comparison to Na and K. These differences arise due to the different path that the Li atom has undertaken while migrating from

one stable site to another during along-belt diffusion. Na and K migrate along the path where “cliff-top” Te atoms are present between adjacent grooves. However, Li chooses a different path, wherein it initially goes through the Te sheet, migrates to the other side, and then come back out of the Te sheet enabling it to avoid encounters with cliff-top Te atoms, leading to a lower energy barrier in comparison with other alkali atoms. Such movement is restricted for Na and K because of their larger size compared to Li; energy barrier for movement through Te is much higher for Na (0.15 eV, Figure S12b, Supporting Information) and K (0.5 eV, Figure S12c, Supporting Information) compared to Li (0.04 eV, Figure S12a, Supporting Information). Once the energy barriers are known, the diffusion constant (D) can be predicted using the Arrhenius equation:

$$D \propto \exp\left(\frac{-E_b}{k_b T}\right) \quad (2)$$

where E_b is the energy barrier, k_b and T are Boltzmann constant and temperature (considering room temperature ≈ 300 K). The ratio of diffusion mobility “across-belt” and “along-belt” is around ≈ 1 for Li, but Na and K diffusion mobility “across-belt” is ≈ 148 times and ≈ 2191 times higher than “along-belt”, respectively. This indicates that the migration of Li atoms on the Te surface is quite isotropic. Given that Te has an anisotropic structure, one would expect non-uniform spatial diffusion for alkali atoms. While such anisotropic diffusion is indeed predicted for Na and K, this is surprisingly not the case for Li.

3.3. Diffusion of Alkali Atoms within Few-Layered Tellurene

To manage the computational cost, we considered a unit cell comprised of three layers of monolayer Te, that were stacked in AB sequence and alkali atoms were placed in the interior of the multilayer stack (Figure S10, Supporting Information). Migration of alkali atoms was studied both “across-belt” and “along-belt” after optimizing the most stable adsorption site in the interior of the stack. When sampling Na and K atoms in the interior of the layered Te, the adjacent layers get deformed, which affects the diffusivity of Na and K. In the case of Li, no such damage was observed. Unlike in single-layer Te, migration of Li atom “across-belt” in layered Te shows two distinct peaks, which are presumably caused by presence of additional binding sites provided by the first layer (Figure 3c). The energy barrier for Li transport was ≈ 0.13 eV, which is much lower than for Na (≈ 0.32 eV; Figure 3d) and K migration (≈ 0.62 eV; Figure 3e). The high energy barrier for Na and K arises due to their much larger atomic size when compared to Li. In addition, the adjacent layers in few-layered Te can provide significant hindrance to restrict the migration of Na and K.

While studying “along-belt” diffusion, a surprising trend in energy barrier was observed in case of Li and Na atoms, wherein the energy barrier first decreases and then increases to a certain value. Such a decrease in energy barrier is likely due to the presence of an even more stable site at the bottom of the first layer as compared to the starting site (local minimum). No such trend was observed for the K atom. As for the single-layered Te case, the energy barrier for Li “along-belt” diffusion

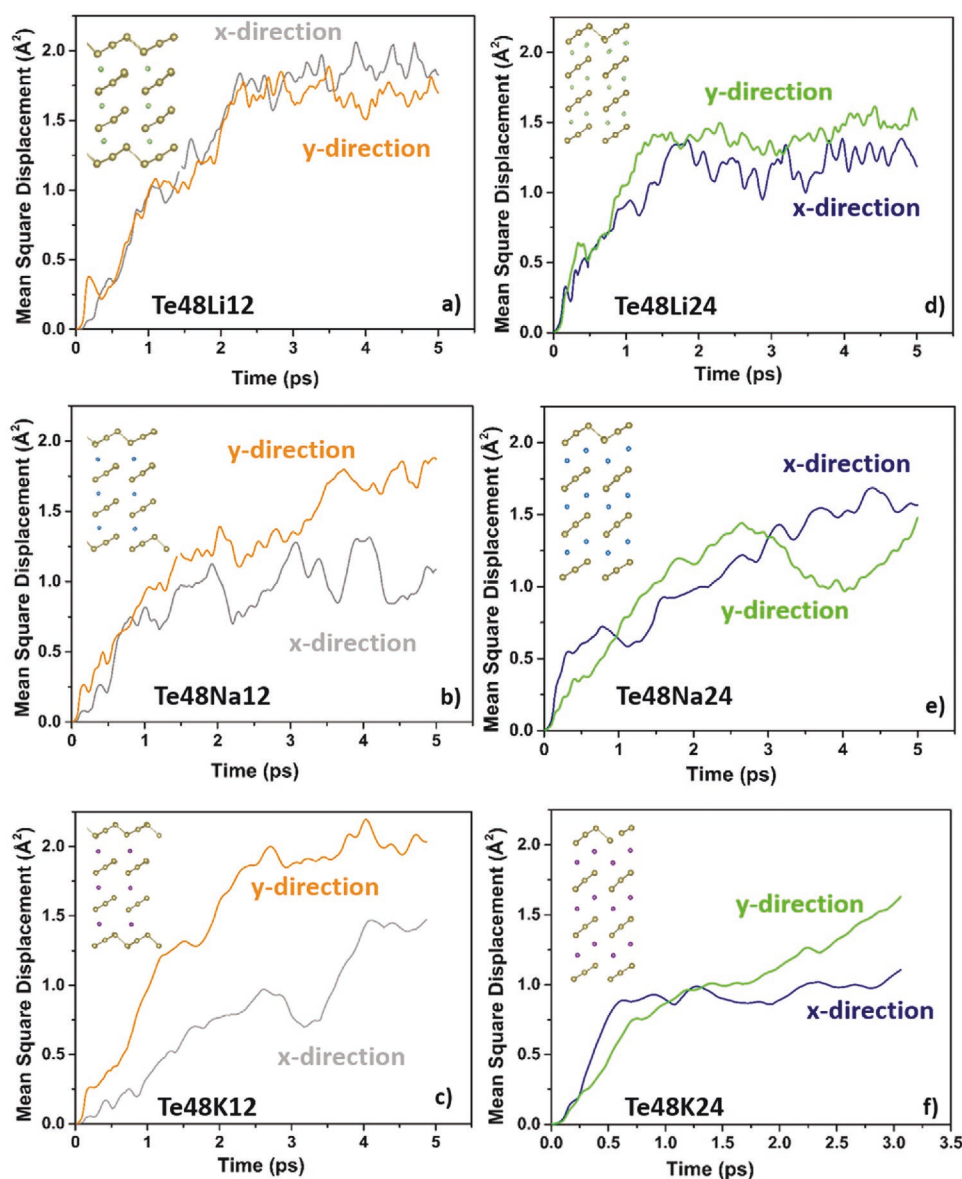


Figure 4. Mean square displacement of alkali ions calculated by ab-initio MD. a–f) Mean square displacement of Li (a,d), Na (b,e), and K (c,f) in $\text{Te}_{48}\text{A}_{12}$ (a–c) and $\text{Te}_{48}\text{A}_{24}$ (d–f) configurations. A denotes an alkali atom (i.e., Li, Na, or K).

for few-layered Te is exactly equal to “across-belt” diffusion (≈ 0.13 eV) and much lower than that of Na (≈ 0.37 eV) and K (≈ 0.67 eV). The lower diffusion energy barrier for Li indicates that Te-based LIBs will have superior high-rate performance when compared with Te-based Na-ion and K-ion batteries. Using the Arrhenius equation, one can show that similar to single-layer Te, the diffusion mobility of Li in few-layered Te is also highly isotropic, whereas Na and K atoms exhibit significantly anisotropic diffusivity.

3.4. Ab-Initio Molecular Dynamics

Since the computational burden of DFT limits its application to larger simulation cells, we utilized AI-MD to explore the

diffusion properties of alkali species in multilayer Te systems. More specifically, $\text{Te}_{48}\text{A}_{12}$ and $\text{Te}_{48}\text{A}_{24}$ ($\text{A} = \text{Li}/\text{Na}/\text{K}$) configurations were used, wherein the $\text{Te}_{48}\text{A}_{12}$ and $\text{Te}_{48}\text{A}_{24}$ structures were initially optimized at 0.1 K and then simulated at 300 K for ≈ 10 ps (Figure S13, Supporting Information) (Experimental Section). As expected, such a high concentration of alkali atoms will start disrupting the 2D Te structure, which is an indication of the onset of the alloying process and if given sufficient time, will lead to the alloyed product. Our main aim during AI-MD was to study the diffusion property of alkali atoms during the alloying process, and to quantify this, we computed the average MSD (Figure 4). While comparing MSD results for $\text{Te}_{48}\text{Li}_{12}$, $\text{Te}_{48}\text{Na}_{12}$, and $\text{Te}_{48}\text{K}_{12}$, we observe that the MSD in the x-direction (across-belt) and y-direction (along-belt) for Li atoms were almost same during the alloying process (Figure 4a). By

contrast, deviation in MSD in x - and y -directions was quite pronounced for Na atoms (Figure 4b) which further increases for K atoms (Figure 4c). In the case of $\text{Te}_{48}\text{Na}_{12}$, and $\text{Te}_{48}\text{K}_{12}$, we observe that the MSD is higher in the y -direction (along-belt) as compared to x -direction (across-belt), which can be due to the lower density of Te–Te bonds along the y -direction. A similar observation was also made when we increased the number of alkali atoms to 24 (Figure 4d–f). Isotropic displacement of Li during the alloying indicates that Li atoms reach every Te atom with equal probability, which leads to the formation of ordered alloyed products. However, in the case of Na and K, one direction of movement is preferred, which indicates that some Te atoms (which lie in a preferred direction) will encounter an abundance of Na or K atoms, while others in a non-preferred direction will experience a scarcity of Na or K atoms. This leads to the unordered formation of the alloyed product, with resultant loss in crystallinity. In this way, the DFT and AI-MD simulation results back up our in situ TEM observations, and provide fundamental insight to explain the differences in the crystalline order of Li_2Te (single-crystal), Na_2Te (poly-crystal), and K_2Te (poly-crystal). Having understood the alloying process of Te with various alkali metals and having developed an in-depth understanding of the alloying phases and compositions, we then proceeded to carry out electrochemical testing of Te-based Li, Na, and K-ion batteries.

3.5. Electrochemical Testing of Tellurene Batteries

A half-cell LIB was assembled by coating Te sheets on a copper foil current collector with a Li metal foil as the counter electrode and 1 M lithium hexafluorophosphate in ethylene carbonate (EC)–diethyl carbonate as the electrolyte. For the half-cell sodium-ion battery (SIB), Na foil was used as counter electrode and the electrolyte was 1 M sodium perchlorate in EC–propylene carbonate (PC), while for the half-cell potassium-ion battery, we employed a K foil with 0.9 M potassium hexafluorophosphate in EC–diethyl carbonate as the electrolyte (Experimental Section). Top and cross-sectional SEM imaging of the electrode indicates that the structure of Te sheets remains intact during the coating process. The typical Te electrode thickness was measured to be ≈ 5 – $10\ \mu\text{m}$ (Figure S14, Supporting Information). It should be noted that the as-prepared electrode has significant non-homogeneous porosity (Figure S14b, Supporting Information). This can be attributed to variation in the lateral dimensions of Te flakes produced by the hydrothermal method (Figure S14a, Supporting Information) as well as variation in thickness of the as-synthesized flakes.

To understand alkali ion insertion, cyclic voltammetry (CV) was performed at a scan rate of $\approx 0.05\ \text{mV s}^{-1}$ over four cycles in the voltage range of 0.03–3 V (for Li), 0.03–2.75 V (for Na), and 0.03–2.5 V (for K). During 1st cycle lithiation process, CV for the Li–Te cell (Figure S15, Supporting Information), shows a prominent peak at $\approx 1.6\ \text{V}$, which is shifted to $\approx 1.65\ \text{V}$ in subsequent cycles. This indicates that the alloying of Te with Li occurs primarily at $\approx 1.65\ \text{V}$. In the first cycle, a prominent peak is also observed at $\approx 1.8\ \text{V}$, but this is related to the solid electrolyte interface (SEI), since it diminishes significantly in subsequent cycles. In the de-lithiation process, a prominent

peak appeared at $\approx 1.97\ \text{V}$ with shoulder peak at $\approx 2.3\ \text{V}$, indicating that the de-alloying reaction occurred at $\approx 1.97\ \text{V}$. Several small and broad peaks were also observed in 0.03–1.5 V range for both reduction and oxidation process which is an indication of step wise lithiation/de-lithiation process. Decrease in current in subsequent cycles is an indication of loss of active material (Te) due to alloying/de-alloying process. Prominent peaks for lithiation/de-lithiation for Te matches with the values of bulk tellurium/1D tellurium.^[3] Similar CV scans for the Na–Te cell and K–Te cell (Figures S16 and S17, Supporting Information) indicate that the alloying reaction of Te with Na takes place primarily at $\approx 1.55\ \text{V}$, while a stepwise de-alloying is observed at ≈ 1.69 and $\approx 2.09\ \text{V}$. For K–Te cell, relatively broad peaks centered at ≈ 1.92 , ≈ 1.03 , and $\approx 0.36\ \text{V}$ during reduction process are observed, which are attributed to stepwise alloying of Te with K, while peaks at ≈ 0.38 , 0.84 , and $\approx 1.94\ \text{V}$, during oxidation process correspond to stepwise de-alloying. The absence of prominent (sharp) peaks for K–Te cells is expected and is attributed to the relatively slow diffusion of K ions due to their larger size. To verify this, we carried out galvanostatic intermittent titration technique (GITT) characterization of the various cells. The measured diffusion coefficient of Li in Te is in the range of 10^{-14} – $10^{-15}\ \text{cm}^2\ \text{s}^{-1}$ which is one order of magnitude higher than Na (10^{-15} – $10^{-16}\ \text{cm}^2\ \text{s}^{-1}$) and two orders higher than K (10^{-16} – $10^{-17}\ \text{cm}^2\ \text{s}^{-1}$) (Figure S18d, Supporting Information). The decrease in reaction resistance and diffusion coefficient at specific voltages, obtained through GITT (Figure S18c,d, Supporting Information), is consistent with the CV results discussed above, which further confirms the alloying of Li/Na/K with Te.

Next, we carried out galvanostatic charge–discharge cycling for the Te-based cells at 0.1C for 50 cycles (Figure S19a, Supporting Information). After 1st cycle (SEI formation step), the Te-based Li cell (Te||Li) showed an initial gravimetric specific capacity of $\approx 350\ \text{mAh g}^{-1}$ (theoretical upper limit for Li_2Te is $\approx 420\ \text{mAh g}^{-1}$). However, a significant drop in specific capacity was observed within the first 20 cycles to $\approx 120\ \text{mAh g}^{-1}$ after which capacity remained fairly constant up to 50 cycles ($\approx 105\ \text{mAh g}^{-1}$). Such rapid capacity fade is common in alloying anodes and is related to volume expansion ($\approx 175.80\%$) in Te, which causes pulverization and delamination of the active material. The capacity fade is even more severe for Na and K. After 50 cycles, Te||Na and Te||K displayed specific capacities of only ≈ 60 and $\approx 42\ \text{mAh g}^{-1}$, respectively. The superior performance of Li over Na and K is understandable given that the volume expansion of Te when alloyed with Na ($\approx 286.5\%$) and K ($\approx 474.74\%$) is much larger than for Li ($\approx 175.80\%$). Corresponding charge/discharge voltage profiles for Te||Li, Te||Na, and Te||K cells show plateaus at similar alloying/de-alloying voltages as observed in CV and GITT measurements and also highlight the capacity fade over 50 cycles (Figure S19b–d, Supporting Information). Initial Columbic efficiency in Te||Li was $\approx 40\%$, which is higher than Te||Na ($\approx 30\%$) and Te||K ($\approx 10\%$). Over 50 cycles, the Columbic efficiency of Te||Li and Te||Na reached $\approx 100\%$, whereas the Columbic efficiency of Te||K was still only $\approx 90\%$. This is presumably due to the larger size of K ($2.8\ \text{\AA}$ vs $1.82\ \text{\AA}$ for Li and $2.22\ \text{\AA}$ for Na), which could impede the de-alloying process. Due to larger size of K ion, during electrochemical impedance spectroscopy (EIS) measurement

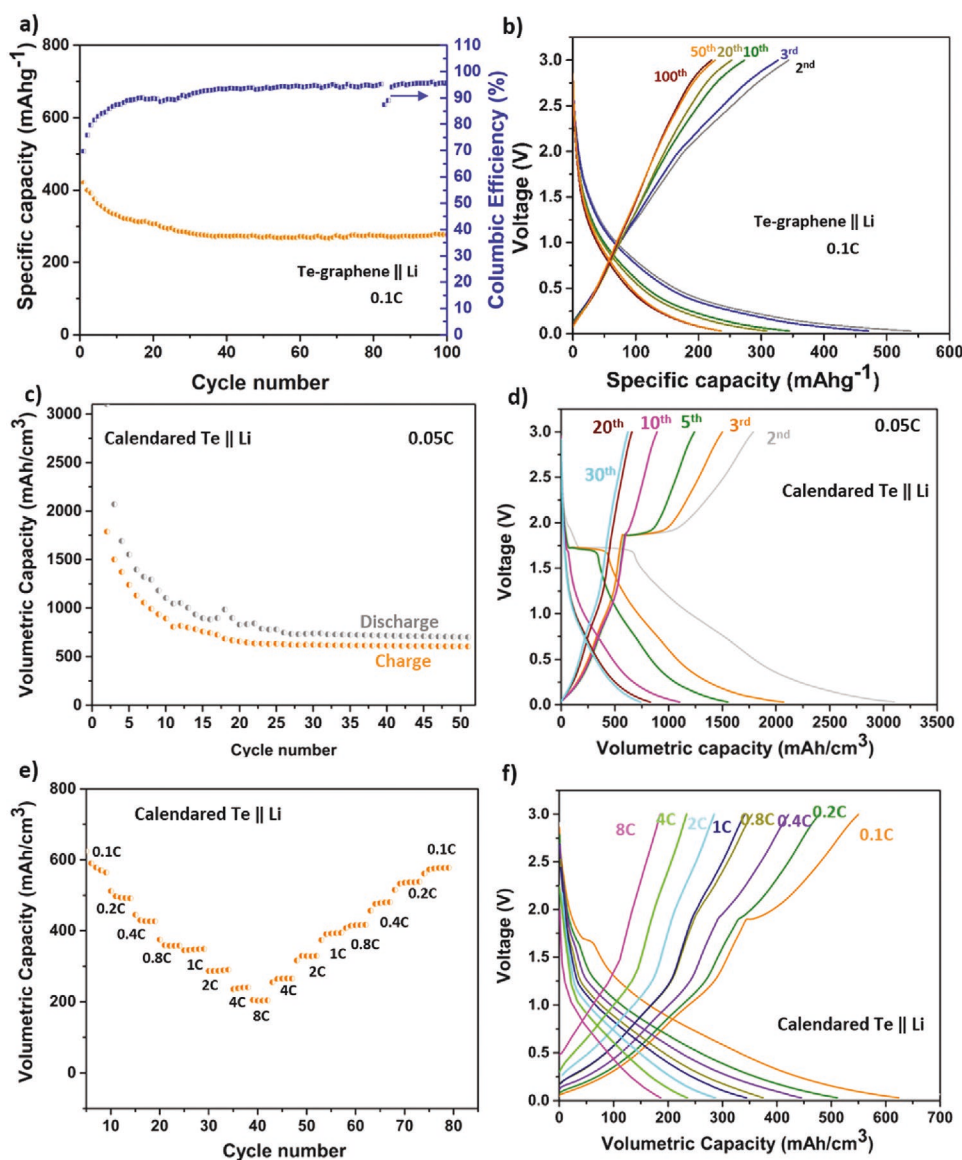


Figure 5. Electrochemical performance of Te. a) Gravimetric performance and Coulombic efficiency of Te in Te-graphene||Li cell at current density of $\approx 0.1C$. b) Electrochemical charge/discharge voltage profile of the Te-graphene||Li cell at a current density of $\approx 0.1C$. c) Volumetric performance of a calendared Te||Li cell at a current density of $\approx 0.05C$. d) Electrochemical charge and discharge voltage profile of the calendared Te||Li cell at a current density of $\approx 0.05C$. e) Effect of charge/discharge rate (C-rate) on volumetric capacity of the calendared Te||Li cell. f) Charge and discharge voltage profiles of the calendared Te||Li cell at various C-rates from 0.1 to 8C. ($1C = 100 \text{ mA g}^{-1}$).

(Experimental Section), Te||K also showed highest resistance, especially charge transfer resistance (semicircle at higher frequency of Nyquist plot), in comparison with Te||Li and Te||Na (Figure S20, Supporting Information).

To address the capacity fade issue, we created composite electrodes of Te with graphene, which displayed much better cycle stability and good rate capability (Figure 5a,b and Figure S21, Supporting Information). This is due to the ability of graphene to act as a buffer layer (42) to suppress the stress induced pulverization and delamination of Te. Figure 5a indicates that Te was able to retain a gravimetric capacity of $\approx 300 \text{ mAh g}^{-1}$ after 100 cycles (calculated after removing contribution of graphene), which demonstrates that the graphene buffering is effective

in mitigating capacity fade. With graphene as a buffer layer, Te was also able to deliver good rate capability (Figure S21c,d, Supporting Information) and showed high cyclic stability ($\approx 400 \text{ mAh g}^{-1}$ at 1C after 850 cycles) (Figure S21e, Supporting Information). The absence of a voltage plateau associated with alloying/de-alloying of Te in Te/graphene (Figure 5b) is related to the large quantity of graphene present in the electrode. Graphene, present in 2:1 mass ratio with Te, dominates the voltage profile and suppresses the voltage plateau associated with Te. However, CV (Figure S21b, Supporting Information) indicates that the Te did undergo alloying/de-alloying reaction even in presence of graphene. CV results show peaks at similar voltages, as was observed in only Te||Li cells ($\approx 1.6 \text{ V}$ during

lithiation process and ≈ 1.9 V during de-lithiation process), corresponding to alloying/de-alloying of Te, which indicates that the alloying/de-alloying of Te successfully takes place in the presence of graphene.

From a gravimetric perspective, Te offers no significant advantage over traditional graphite. However, volumetrically the picture is very different. The theoretical maximum volumetric capacity of Te in LIBs is $\approx 2620 \text{ mAh cm}^{-3}$ which is ≈ 6 –8 times higher than graphite. To maximize volumetric capacity, we performed calendaring (Experimental Section) to densify the Te electrode and avoided the use of graphene as a buffering material. Graphene, as a composite material and if present in considerable amount, curtails the volumetric capacity of the electrode because of its much lower theoretical volumetric capacity (≈ 330 – 430 mAh cm^{-3}) compared to Te. Hence, we investigated the volumetric capacity of Te without using any graphene buffer material. Calendaring of Te decreased the electrode thickness by five-to-tenfold (≈ 1 – $2 \text{ }\mu\text{m}$) as evidenced by cross-sectional SEM (Figure S22, Supporting Information) and energy dispersive X-ray analysis (Figure S23, Supporting Information). Calendaring also greatly reduced the non-homogeneous porosity of the material and resulted in a compact/dense electrode structure (Figure S22b, Supporting Information). The calendared Te electrode showed a high initial volumetric charge capacity of $\approx 1800 \text{ mAh cm}^{-3}$ ($\approx 300 \text{ mAh g}^{-1}$). In the absence of the graphene buffering material, capacity fade during initial cycles is unavoidable. In spite of this, the volumetric capacity stabilizes to $\approx 700 \text{ mAh cm}^{-3}$ ($\approx 115 \text{ mAh g}^{-1}$) after 50 cycles (Figure 5c) which is approximately twice that of commercial graphitic anodes (330 – 430 mAh cm^{-3}).^[17] The capacity fade could possibly be mitigated (without compromising on volumetric performance) by chemical vapor or atomic layer deposition coating of the individual Te flakes with an appropriate ultrathin buffering material and should be pursued as part of future work. It should be noted that the volumetric capacity numbers reported here are based on the volume of the “entire electrode” including the active (Te) material, carbon black, and binder. The low (initial) Columbic efficiency of the Te electrode is attributed to pulverization and delamination of the electrode due to large volume expansion, which exposes new surface for the electrolyte to react and form the SEI. This leads to low Columbic efficiency, which is a common problem in most alloying-based anodes. However, it should be noted that after about 20 cycles, the electrode response is relatively stable (Figure 5c), which allows the cell to reach a Columbic efficiency of $\approx 95\%$. The voltage profile for the calendared Te electrode (Figure 5d) shows similar plateaus at the same voltages as what was observed for the non-calendared Te (Figure S19b, Supporting Information), confirming that the alloying/de-alloying process is unaffected by calendaring. The observed potential profiles are indicative of stepwise alloying of Te as well as interfacial-charge storage in Te. The weakening of the prominent alloying plateau for the calendared Te electrode after ten cycles can be attributed to the constant delamination/pulverization of the electrode material due to volume expansion, which results in significant loss of active material, leading to a suppressed alloying plateau.

The rate capability of the calendared Te electrodes was also investigated by running cells over a wide range of current

densities (0.1–8C) (Figure 5e,f). After initial decay in volumetric capacity in first five cycles due to electrode pulverization, the calendared Te showed quite stable volumetric capacity of ≈ 400 , 375, and 350 mAh cm^{-3} at 0.4, 0.8, and 1C, respectively. Even at higher current density, Te was able to show volumetric capacity of ≈ 225 and 200 mAh cm^{-3} at 4 and 8C, respectively. These results indicate that Te offers good high-rate performance, which can be attributed to its thin 2D flake structure, which reduces Li-ion diffusion distances and enables efficient charge transport. In case of high-rate testing, sufficient time is not available for Te to react completely with Li, leading to the absence of a prominent alloying plateau in the voltage profiles.

4. Conclusion

To summarize, we have reported alloying of a range of alkali metals (A = Li, Na or K) with few-layer Te. In situ TEM and DFT indicated that Te alloys with alkali metals forming A_2Te . However, the crystalline order varied significantly from single-crystal (for Li_2Te) to poly-crystal (for Na_2Te and K_2Te). Simulations reveal that compared to Na or K, migration of Li is highly “isotropic” in Te. Such isotropic transport is made possible by Te’s peculiar structure comprised of chiral-chains bound by vdW interactions. Isotropic displacement of Li indicates that Li atoms reach every Te atom with equal probability, which leads to formation of ordered alloy products. However, in the case of Na and K, one direction of movement is preferred, indicating that some Te atoms (which lie in a preferred direction) will encounter an abundance of Na or K atoms, while others in a non-preferred direction will experience a scarcity of Na or K atoms. This leads to the unordered formation of the alloyed product, with resultant loss in crystallinity. This explains why the single-crystal Te maintains its crystalline identity when reacted with Li, but fails to do so when alloyed with Na or K.

Another key observation was that Te when alloyed with alkali metals undergoes huge volume expansion which leads to delamination and pulverization of the electrodes. Improved methods to conformally coat Te with carbon-based buffering materials as well as electrolyte engineering to create flexible and mechanically robust SEI layers should therefore be explored as part of future work. From a gravimetric perspective, Te cannot significantly outperform graphite due to its high atomic mass. That being said, there are many applications (such as grid storage or portable electronics) where volumetric performance is far more relevant than gravimetric numbers. In such applications, Te can significantly outperform graphite. We find that when alloyed with Li, Te exhibited a stable volumetric capacity of $\approx 700 \text{ mAh cm}^{-3}$, about twice the practical capacity of commercial graphite. Such Te-based electrodes show significant potential for LIB applications involving energy storage in compact spaces, where the maximum amount of energy must be packed into a limited volume.

5. Experimental Section

Tellurene Material Synthesis: A one-step hydrothermal method was used to synthesize Te.^[2] Initially, $\approx 100 \text{ mg}$ of sodium tellurite (Na_2TeO_3)

and ≈ 345 mg of polyvinyl pyrrolidone (PVP, k17) were mixed in ≈ 33 mL of de-ionized water at room temperature for ≈ 10 min followed by addition of ≈ 1 mL hydrazine hydrate (N_2H_4 , 85% wt/wt%) and ≈ 2 mL ammonia solution (NH_4 25% wt/wt%). The mixture was then transferred to a Teflon lined stainless steel autoclave (50 mL) which was then heated at $\approx 180^\circ\text{C}$ for ≈ 40 h. This led to the formation of a silver-grey colored powder, which was washed several times with de-ionized water using filtration method to remove any ion contaminants. To remove PVP molecules adsorbed on the Te surface, acetone (≈ 3 mL) was added to the Te solution (≈ 1 mL) and kept for several hours at room temperature. The solution was then washed several times with de-ionized water to obtain the purified 2D Te sheets.

Tellurene Electrode Synthesis: Only Te-based electrode was synthesized by mixing Te with super P carbon black and polyvinylidene fluoride (PVDF) binder in 70:20:10% proportion by weight. Few drops of NMP were carefully added into the mixture which was then stirred for ≈ 20 min at ≈ 2000 rpm. This led to the formation of silver-grey colored slurry, which was coated over a copper foil current collector substrate and dried overnight at room temperature. Te-graphene electrode was synthesized using a similar procedure with an alteration in a weight proportion wherein composition of electrode was 80:10:10% (Te/graphene:C-black:PVDF).

Calendaring was done using MTI-MSK_HRP MR100DC machine, wherein as-fabricated electrodes were placed in between moving rollers (rotating at minimum speed). To obtain uniform thickness, calendaring was repeated multiple times. Calendaring process densified the electrodes by filling all the pores present in the non-calendared Te.

Tellurene/Graphene Synthesis: To synthesize Te/graphene composites, as fabricated Te was mixed in anhydrous NMP (≈ 0.5 mg mL^{-1}) and was bath sonicated for ≈ 30 min. Similarly, single-layer graphene (ACS Materials) was also mixed in anhydrous NMP (≈ 1 mg mL^{-1}) followed by bath sonication for ≈ 30 min. Later, both solutions were mixed, and further bath sonicated for ≈ 1 h which lead to fabrication of Te/graphene composite. The resultant product was filtered and then dried at $\approx 70^\circ\text{C}$ under vacuum overnight which leads to the removal of any NMP traces. This led to formation of the Te-graphene composite powder. The mass ratio of graphene to Te was kept at ≈ 2.0 .

Lithium, Sodium, and Potassium Half-Cell Measurements: 2032-type coin cells were assembled wherein Li, Na, and K metal was used as a reference electrode for Li, Na, and K half-cell measurement, respectively. Initially, as-prepared electrodes were punched into circular disks with an area of ≈ 1.27 cm^2 . Mass loading (Te + carbon black + PVDF) ranged from 0.75 to 1.25 mg cm^{-2} . In case of Li cells, commercially available 1.0 M lithium hexafluorophosphate (LiPF_6) in EC: diethyl carbonate (DEC), 1:1 volume ratio, was used as the electrolyte. In the case of K cells, 0.9 M potassium hexafluorophosphate (KPF_6) in EC: DEC (1:1 v/v) was synthesized and used as an electrolyte.^[32] 1.0 M sodium perchlorate (NaClO_4) in EC: PC (1:1 v/v) was synthesized and used as an electrolyte for Na cells. Sodium perchlorate in EC:PC was considered to perform better in comparison with other standard electrolytes for SIBs.^[33] Celgard 2340 polypropylene membrane was used as a separator for both Li and K cells, whereas a Whatman glass fiber membrane was used for Na cells since the Celgard 2340 polypropylene membrane did not wet the EC:PC solvent. All cells were assembled in an argon-filled glove box (MBraun Labster) with moisture and oxygen level <0.1 ppm. Charge/Discharge measurement was done using Arbin BT200 battery test equipment and within voltage window of 0.03–3, 0.03–2.75, and 0.03–2.5 V for Li, Na, and K cells, respectively. GITT was also performed using the same equipment and voltage window. For GITT measurement, in all three cells, 2D Te anode was initially activated by running the cells in their corresponding voltage range at 0.1C for at least 2–3 cycles. Following that, pulse current was provided each hour after long relaxation time of 5 h, which provided quasi-circuit-open potential (Figure S18a,b, Supporting Information). Reaction resistance in all three cells was calculated at each relaxation-pulse step by dividing overpotential with pulse current density (Figure S18c, Supporting Information). Gamry instrument was used to perform CV and EIS of all the cells in their respective voltage windows. After activating the Te||Li, Te||Na, and Te||K

for three cycles at 0.1C, EIS was performed in the frequency range of 0.01Hz–100kHz.

Calculation Details: All the DFT computations were carried out with the Vienna Ab-initio Simulation Package (VASP) using the projector-augmented-wave (PAW) method.^[34–36] The exchange-correlation effects were described by the Perdew–Burke–Ernzerhof (PBE) functional within the generalized gradient approximation (GGA).^[37] To account for the vdW interactions resulting from the fluctuating charge distributions, Grimme's empirical dispersion correction scheme was employed (DFT-D3 method in VASP).^[38] A kinetic energy cutoff of 500 eV was used to generate a plane-wave basis set and k-points were sampled using a gamma point centered $4 \times 4 \times 1$ Monkhorst–Pack mesh.^[39] The geometry optimization was run until the self-consistent field (SCF) energies and maximum forces on each atom were below a threshold value of 10^{-5} and 0.05 $\text{eV}\text{\AA}^{-1}$, respectively. The conjugate gradient algorithm was utilized to relax all structures. In this work, the authors consider a monolayer (48 Te atoms) and a four-layer (36 Te atoms) α tellurene supercell. The supercell dimensions for the four-layer Te system in x- and y-directions were 8.86 and 11.87 \AA , respectively. However, for the monolayer system, cell dimensions were relatively larger with $x = 17.72$ \AA and $y = 23.73$ \AA , and only the gamma point was considered for the calculation. A vacuum of over 15 \AA in the z-direction was used to avoid unwanted interaction between periodic images. To understand the diffusion of alkali (Li/Na/K) atoms in monolayer/four-layer Te, DFT in conjunction with climbing image NEB^[40,41] method was used to investigate the migration paths and energy barriers of alkali atom moving from one stable site to another in x-/y- or along the z-directions. Further, Hirschfeld-I charges was evaluated to understand the charge distribution or transfer during Li/Na/K atom binding with the Te surfaces.

Ab-Initio Molecular Dynamics Calculations: The AI-MD simulations were performed using the VASP. First, the lattice constants of the configurations studied, namely: $\text{Te}_{48}\text{Li}_{12}$, $\text{Te}_{48}\text{K}_{12}$, $\text{Te}_{48}\text{Na}_{12}$, $\text{Te}_{48}\text{Li}_{24}$, $\text{Te}_{48}\text{K}_{24}$, and $\text{Te}_{48}\text{Na}_{24}$, were optimized through energy minimization. The structures were then relaxed by initial geometry optimization through DFT calculations, which was followed by the AIMD run. To study the directional diffusion characteristics, MSD of the diffusing Li, K, and Na atoms was calculated from AIMD trajectories sampled for runtimes of 5 ps. An isokinetic ensemble (NVT) was adopted for the simulations, where the ionic temperature (300 K) was controlled by the Nose–Hoover thermostat. A time step of 1 fs was used for the integration of the equations of motion. The authors used PAW_PBE pseudopotential for the calculations. The ion–electron interactions were presented with the PAW method, and the exchange-correlation effects were determined by the GGA with the PBE functional. An energy cutoff of 350 eV was considered for the plane-wave basis and a $4 \times 4 \times 1$ Monkhorst–Pack scheme k-point grid was adopted for the systems studied. The structural relaxation was performed using the conjugated gradient minimization method to make sure the force on each atom was less than 0.05 $\text{eV}\text{\AA}^{-1}$. A shortcoming with the standard DFT-AIMD approach was the unreliable representation of the vdW interaction. To overcome this, the authors used dispersion correction method proposed by Grimme,^[42] which incorporates the vdW interactions missing in the standard calculations by taking into account a pairwise interatomic term C_6R^{-6} to the DFT energy.

In Situ Transmission Electron Microscopy Measurement: Preparation of Te and Li electrodes were done using Nanofactory STM in situ holder with its chip region featuring two dangling metallic (Au or W) tips. To load the Li metal anode, the metallic tip was used to scratch the surface of one Li metal foil inside a glove box. A small amount of Li metal was then attached to the tip surface. Another metallic tip was dipped into the Te nanoflake powder to grab certain amount of Te on the tip surface as the working electrode. The two tips were then taken out of the glove box and transferred into the TEM chamber after exposure to atmosphere for about 30 s. Such short exposure time leads to the formation of a thin oxide layer on the surface of Li metal anode, which was electron-insulating but Li^+ conducting and could be thus regarded as a solid-state electrolyte, as reported in the authors' previous work.^[43,44] A constant bias voltage (≈ 3 V) was applied to initiate insertion of Li^+ into Te. Similar

procedures were repeated for in situ TEM study of alloying behavior between Na/K and Te. The above experimental procedure for in situ TEM study of battery materials had been widely explored and reported to be reliable in terms of revealing the working mechanisms of electrode material of interest.^[45]

Materials Characterization: Morphology of Te sheets and electrodes were obtained using Carl Zeiss Supra 55 field-emission scanning electron microscope with beam energy of ≈ 2.5 kV. Cross section of the Te electrodes before and after calendaring was obtained using gallium focused ion beam sputtering^[46] at ≈ 30 keV using FEI VERSA 3D dual beam system. Coarse sputtering and final cleaning of the cross section were carried out at ≈ 15 and ≈ 1 nA beam current, respectively. Deposition of platinum through ion beam allowed the authors to protect the electrode surface from damage due to sputtering at higher ion beam current. SEM images of cross section were taken at ≈ 2.5 kV and at an $\approx 52^\circ$ tilt. TEM was done using JEM2100F operating at 200 kV. STEM-EDS mapping was done using EOL JEMARM200CF equipped with a 200 kV cold field emission electron gun and an Oxford X-max 100TLE windowless SDD X-ray detector. Thickness of as-synthesized Te was obtained through AFM (Bruker, Innova). Raman spectroscopy was obtained through back scattering geometry using a single monochromator with a Renishaw in via microscope equipped with cooled (-70°C) CCD array detector (1024×256 pixels) and edge filter. XRD data was obtained through Bruker D2 PHASER using Cu/K α radiation ($\lambda = 1.5418 \text{ \AA}$) at 40 kV and 30 mA. XPS was obtained using PHI 5000 versa probe system using Al K α radiation ($\approx 1486 \text{ eV}$).

Supporting Information

Supporting Information is available from the Wiley Online Library or from the author.

Acknowledgements

R.J. and Y.Y. contributed equally to this work. This work was supported by the USA National Science Foundation (award numbers 1922633, 2013640, 2002742, and 2015750). N.K. acknowledges funding support from the John A. Clark and Edward T. Crossan endowed chair professorship at Rensselaer Polytechnic Institute (RPI). S.O.K. was financially supported by the National Creative Research Initiative (CRI) Center for Multi-Dimensional Directed Nanoscale Assembly (2015R1A3A2033061) through the National Research Foundation of Korea (NRF). R.S.-Y. and Y.Y. acknowledge the financial support from NSF CBET-1805938. This work made use of instruments in the Electron Microscopy Service (Research Resources Center, UIC). L.-W.W. acknowledges support from Assistant Secretary for Energy Efficiency and Renewable Energy of the U. S. Department of Energy under Battery Materials Research (BMR) program. The theoretical work in this research used the resources of the National Energy Resources Scientific Computing Center (NERSC) that is supported by the Office of Science of the U. S. Department of Energy. D.M. is supported by the USA National Science Foundation, Division of Materials Research, Award No. 1938833.

Conflict of Interest

The authors declare no conflict of interest.

Keywords

alloying, crystallinity, tellurene, volumetric capacity

Received: October 12, 2020

Revised: November 26, 2020

Published online: December 27, 2020

- [1] Y. Wang, G. Qiu, R. Wang, S. Huang, Q. Wang, Y. Liu, Y. Du, W. A. G. Iii, M. J. Kim, X. Xu, P. D. Ye, W. Wu, *Nat. Electron.* **2018**, 1, 228.
- [2] D. Wang, A. Yang, T. Lan, C. Fan, J. Pan, Z. Liu, J. Chu, H. Yuan, X. Wang, M. Rong, N. Koratkar, *J. Mater. Chem. A* **2019**, 7, 26326.
- [3] Y. Liu, J. Wang, Y. Xu, Y. Zhu, D. Bigio, C. Wang, *J. Mater. Chem. A* **2014**, 2, 12201.
- [4] J.-U. Seo, G.-K. Seong, C.-M. Park, *Sci. Rep.* **2015**, 5, 7969.
- [5] W. Wu, G. Qiu, Y. Wang, R. Wang, P. Ye, *Chem. Soc. Rev.* **2018**, 47, 7203.
- [6] S. Sharma, N. Singh, U. Schwingenschlög, *ACS Appl. Energy Mater.* **2018**, 1, 1950.
- [7] S. Deckoff-Jones, Y. Wang, H. Lin, W. Wu, J. Hu, *ACS Photonics* **2019**, 6, 1632.
- [8] R. Jain, Y. Singh, S.-Y. Cho, S. P. Sasikala, S. H. Koo, R. Narayan, H.-T. Jung, Y. Jung, S. O. Kim, *Chem. Mater.* **2019**, 31, 2786.
- [9] R. Jain, R. Narayan, S. P. Sasikala, K. E. Lee, H. J. Jung, S. O. Kim, *2D Mater.* **2017**, 4, 042006.
- [10] Q. Li, Q. Zhou, L. Shi, Q. Chen, J. Wang, *J. Mater. Chem. A* **2019**, 7, 4291.
- [11] J. Yan, H. Pang, L. Xu, J. Yang, R. Quhe, X. Zhang, Y. Pan, B. Shi, S. Liu, L. Xu, J. Yang, F. Pan, Z. Zhang, J. Lu, *Adv. Electron. Mater.* **2019**, 5, 1900226.
- [12] C. K. Chan, H. Peng, G. Liu, K. Mcllwraith, X. F. Zhang, R. A. Huggins, Y. Cui, *Nat. Nanotechnol.* **2008**, 3, 31.
- [13] M. T. Janish, D. T. Mackay, Y. Liu, K. L. Jungjohann, C. B. Carter, M. G. Norton, *J. Mater. Sci.* **2016**, 51, 589.
- [14] W. Xia, Q. Zhang, F. Xu, H. Ma, J. Chen, K. Qasim, B. Ge, C. Zhu, L. Sun, *J. Phys. Chem. C* **2016**, 120, 5861.
- [15] X. H. Liu, J. W. Wang, S. Huang, F. Fan, X. Huang, Y. Liu, S. Krylyuk, J. Yoo, S. A. Dayeh, A. V. Davydov, S. X. Mao, S. T. Picraux, S. Zhang, J. Li, T. Zhu, J. Y. Huang, *Nat. Nanotechnol.* **2012**, 7, 749.
- [16] T. Yang, H. Ke, Q. Wang, Y. Tang, Y. Deng, H. Yang, X. Yang, P. Yang, D. Ling, C. Chen, Y. Zhao, H. Wu, H. Chen, *ACS Nano* **2017**, 11, 10012.
- [17] N. Nitta, F. Wu, J. T. Lee, G. Yushin, *Mater. Today* **2015**, 18, 252.
- [18] Z. Tang, Y. Wang, K. Sun, N. A. Kotov, *Adv. Mater.* **2005**, 17, 358.
- [19] M. Safdar, X. Zhan, M. Niu, M. Mirza, Q. Zhao, Z. Wang, J. Zhang, L. Sun, J. He, *Nanotechnology* **2013**, 24, 185705.
- [20] Q. Wang, M. Safdar, K. Xu, M. Mirza, Z. Wang, J. He, *ACS Nano* **2014**, 8, 7497.
- [21] J. Chen, Y. Dai, Y. Ma, X. Dai, W. Ho, M. Xie, *Nanoscale* **2017**, 9, 15945.
- [22] X. Huang, J. Guan, Z. Lin, B. Liu, S. Xing, W. Wang, J. Guo, *Nano Lett.* **2017**, 17, 4619.
- [23] Z. Xie, C. Xing, W. Huang, T. Fan, Z. Li, J. Zhao, Y. Xiang, Z. Guo, J. Li, Z. Yang, B. Dong, J. Qu, D. Fan, H. Zhang, *Adv. Funct. Mater.* **2018**, 28, 1705833.
- [24] Y. Xiang, S. Gao, R.-G. Xu, W. Wu, Y. Leng, *Nano Energy* **2019**, 58, 202.
- [25] S. C. Jung, J. W. Choi, Y.-K. Han, *Nano Lett.* **2012**, 12, 5342.
- [26] T. Shang, Y. Wen, D. Xiao, L. Gu, Y.-S. Hu, H. Li, *Adv. Energy Mater.* **2017**, 7, 1700709.
- [27] Q. Su, J. Xie, J. Zhang, Y. Zhong, G. Du, B. Xu, *ACS Appl. Mater. Interfaces* **2014**, 6, 3016.
- [28] J. Moon, M.-S. Park, M. Cho, *ACS Appl. Mater. Interfaces* **2019**, 11, 19183.
- [29] C. Wang, J. Wen, F. Luo, B. Quan, H. Li, Y. Wei, C. Gu, J. Li, *J. Mater. Chem. A* **2019**, 7, 15113.
- [30] X. Fan, W. T. Zheng, J.-L. Kuo, D. J. Singh, *ACS Appl. Mater. Interfaces* **2013**, 5, 7793.
- [31] C. Ling, F. Mizuno, *Phys. Chem. Chem. Phys.* **2014**, 16, 10419.
- [32] R. Jain, P. Hundekar, T. Deng, X. Fan, Y. Singh, A. Yoshimura, V. Sarbada, T. Gupta, A. S. Lakhot, S. O. Kim, C. Wang, N. Koratkar, *ACS Nano* **2019**, 13, 14094.

- [33] A. Ponrouch, E. Marchante, M. Courty, J.-M. Tarascon, M. R. Palacín, *Energy Environ. Sci.* **2012**, 5, 8572.
- [34] G. Kresse, D. Joubert, *Phys. Rev. B* **1999**, 59, 1758.
- [35] G. Kresse, J. Furthmüller, *Comput. Mater. Sci.* **1996**, 6, 15.
- [36] P. E. Blöchl, *Phys. Rev. B* **1994**, 50, 17953.
- [37] J. P. Perdew, K. Burke, M. Ernzerhof, *Phys. Rev. Lett.* **1996**, 77, 3865.
- [38] S. Grimme, J. Antony, S. Ehrlich, H. Krieg, *J. Chem. Phys.* **2010**, 132, 154104.
- [39] H. J. Monkhorst, J. D. Pack, *Phys. Rev. B* **1976**, 13, 5188.
- [40] G. Henkelman, B. P. Uberuaga, H. Jónsson, *J. Chem. Phys.* **2000**, 113, 9901.
- [41] G. Henkelman, H. Jónsson, *J. Chem. Phys.* **2000**, 113, 9978.
- [42] S. Grimme, *J. Comput. Chem.* **2006**, 27, 1787.
- [43] Y. Yuan, G. Tan, J. Wen, J. Lu, L. Ma, C. Liu, X. Zuo, R. Shahbazian-Yassar, T. Wu, K. Amine, *Adv. Funct. Mater.* **2018**, 28, 1706443.
- [44] Y. Yuan, L. Ma, K. He, W. Yao, A. Nie, X. Bi, K. Amine, T. Wu, J. Lu, R. Shahbazian-Yassar, *Nano Energy* **2016**, 19, 382.
- [45] Y. Yuan, K. Amine, J. Lu, R. Shahbazian-Yassar, *Nat. Commun.* **2017**, 8, 15806.
- [46] J. Dang, F. Xiang, N. Gu, R. Zhang, R. Mukherjee, I. Oh, N. Koratkar, Z. Yang, *J. Power Sources* **2013**, 243, 33.